# Noninvasive time-lapse 3D subcellular analysis of embryo development for machine learning-enabled prediction of blastocyst formation

Chungha Lee[1,2], Geon Kim[1,2], Taeseop Shin[3], Sangho Lee[3], Jae Young Kim[3], Kyoung Hee Choi[3], Jieun Do[4], Jaehyeong Park[5], Jaephil Do[5], Ji Hyang Kim[3*], and YongKeun Park[1,2,5*]

[1]*Department of Physics, Korea Advanced Institute of Science and Technology (KAIST), Daejeon, 34141, Republic of Korea*

[2]*KAIST Institute for Health Science and Technology, KAIST, Daejeon, 34141, Republic of Korea*

[3]*Fertility Center of CHA Bundang Women's Medical Center, Seongnam, 13496, Republic of Korea*

[4]*KAIST Laboratory Animal Resource Center, Daejeon, 34141, Republic of Korea*

[5]*Tomocube Inc., Daejeon 34109, Republic of Korea*

**E-mails: bin0902@chamc.co.kr and yk.park@kaist.ac.kr*

**Abstract**

In developmental biology and in vitro fertilization (IVF), image-based assessment of embryos is pivotal. Traditional methods in clinical IVF have been constrained to 2D morpho-kinetic profiling and manual selection, hindered by the absence of noninvasive techniques for quantitative 3D imaging over extended durations. Here, we overcome these limitations by employing low-coherence holotomography to monitor mouse preimplantation embryo development from the 2-cell stage to the expanded blastocyst. This approach enables the generation of 3D refractive index tomograms of unlabeled embryos, facilitating the observation of subcellular developmental dynamics. We investigated the 3D spatiotemporal profiles of embryo development, identifying key morpho-kinetic parameters that distinguish between embryos with differing developmental outcomes—specifically, Grade A embryos that successfully progressed to expanded blastocysts within 72 hours, and Grade C embryos that did not. Using machine learning, we demonstrate the 3D morpho-kinetic parameters can offer a noninvasive, quantitative framework for predicting embryos with high developmental potential.

## Introduction

Despite the global rise in Assisted Reproduction Technology (ART) procedures, success rates linger below 25%[1]. Enhancing ART's efficacy hinges on precise embryo quality assessment. Currently, *in vitro* fertilization (IVF) predominantly employs morphological evaluation of embryos on day 5[2,3]. Though widely used, this method falls short of capturing the dynamic evolution of embryo development. The advent of noninvasive time-lapse imaging has been introduced, offering a detailed observation of early embryo development stages[4]. This approach has led to the identification of morpho-kinetic parameters that provide a dataset for assessing embryo viability, thereby refining embryo selection criteria[5,6]. However, the assessment of embryo quality through imaging is based on 2D morpho-kinetic profiling, largely due to a shortfall in non-invasive techniques capable of high-resolution, whole-embryo optical sectioning. While 3D fluorescence microscopy offers detailed subcellular views of embryo development, its requirement for fluorescent staining renders it unsuitable for clinical IVF use[7-11]. Consequently, label-free microscopy

techniques, including bright-field, dark-field, and Hoffman modulation contrast microscopy[4], have become the standard in noninvasive embryo imaging for clinical settings. Nonetheless, these methods provide only 2D and qualitative representations of inherently 3D structures, potentially compromising the precision of embryo quality assessments.

To overcome these challenges, quantitative, label-free 3D imaging techniques present a promising solution. Quantitative phase imaging (QPI), which leverages the refractive index (RI) for intrinsic imaging contrast, offers a non-destructive approach to visualize unlabeled samples without the risks of phototoxicity or photobleaching, thus allowing extended observation times[12]. QPI has been applied across a wide range of fields, including cell biology[13-15], microbiology[16-18], immunology[19-21], and biophysics[22,23]. Among these, holotomography (HT), a 3D QPI technique, has proven effective for analyzing thick samples, such as 3D cell-culture models[24-26], thick tissues[27-29], and embryos[30-34] from various species including *C.elegans*[33], Bovine[31], pig[32,35], and mouse embryos[34,36]. Despite HT's evident potential in developmental biology, previous studies have yet to delve into the 3D subcellular intricacies of early embryo development.

Here, we present a systematic approach to investigate embryogenesis. We present the label-free high-resolution 3D imaging of embryo developments and, utilizing low-coherence HT and comprehensive machine learning-enabled analysis for the accurate, noninvasive assessment of embryo quality. By capturing high-resolution 3D RI tomograms at various stages from the 2-cell stage through to the expanded blastocyst, we correlate specific developmental trajectories with initial subcellular configurations. Our investigation identifies a set of parameters at both cellular and subcellular levels, revealing physiological insights into early embryo development. Differences in the 3D spatial arrangement and RI values of blastomeres, nuclei, and cytoplasmic granules were observed between embryos at different cleavage stages, correlating with distinct developmental outcomes. Leveraging these observations, we propose a predictive model for blastocyst formation based on 3D morpho-kinetic parameters, underscoring the potential of utilizing subcellular characteristics for enhancing noninvasive biomarkers of embryo quality.

## Results

### Time-lapse low-coherence HT of *in vitro* embryo development

We first present the capability of low-coherence HT for conducting high-resolution 3D time-lapse imaging of mouse embryo development *in vitro*. Our methodological framework unfolds in three primary phases (Fig. 1a): (i) culturing embryos through conventional IVF and gathering 2-cell stage embryos; (ii) executing 3D time-lapse imaging from the 2-cell stage to the expanded blastocyst over a span of 72 hours; and (iii) carrying out noninvasive analyses and evaluations of the embryos. In the process of low-coherence HT, we collected multiple intensity images across four optimized illumination patterns, combined with axial sample scanning[37]. This was followed by a 3D deconvolution process of the intensity images stack to form the 3D RI image of each embryo. Significantly, our imaging technique employs red light with a peak wavelength of 624 nm, acknowledged for its safety in embryo assessments[38]. Validation of our approach was further substantiated by comparing blastocyst rates between HT-imaged and traditionally cultured embryos, which were 89.34±8.92% and 85.15±2.92% respectively (Fig. 1b). These rates satisfy the FDA's guidelines for mouse embryo assays in ART devices[39], affirming the utility of our method. Further insights into embryo culture practices and the specifics of low-coherence HT are detailed in the Methods section.

Figures 1c and d illustrate the 3D rendered (the maximum intensity projection) and XY-sectioned RI maps of time-lapse HT images capturing the development of mouse embryos (Supplementary Movie 1). The 3D renderings effectively showcase the spatial configuration of blastomeres within the embryo, while

the XY-sectioned RI maps provide detailed insights into the embryo's internal structures. Notably, at the initial 2-cell stage, the distinct positioning of the two blastomeres and a polar body across different focal planes is clearly visible (indicated by yellow arrows in Fig. 1d at t = 0 h). This level of detail facilitates the identification and accurate size measurement of multiple blastomeres at their respective focal planes, crucial for standard embryo assessment processes (observed at t = 24 h in Fig. 1d). As the embryos proceed through cell compaction, the nuclei and nucleoli are distinctly imaged in three dimensions (highlighted at t = 36 h and t = 48 h in Fig. 1d, yellow arrows). By t = 60 h post-2-cell stage, the formation of a cavity within the embryo is observed (marked by the yellow arrow in Fig. 1d at t = 60 h). Our method's superior optical sectioning capability enables comprehensive imaging of the entire 3D structure of the expanded blastocyst, capturing subcellular details at t = 72 h in Fig. 1d.

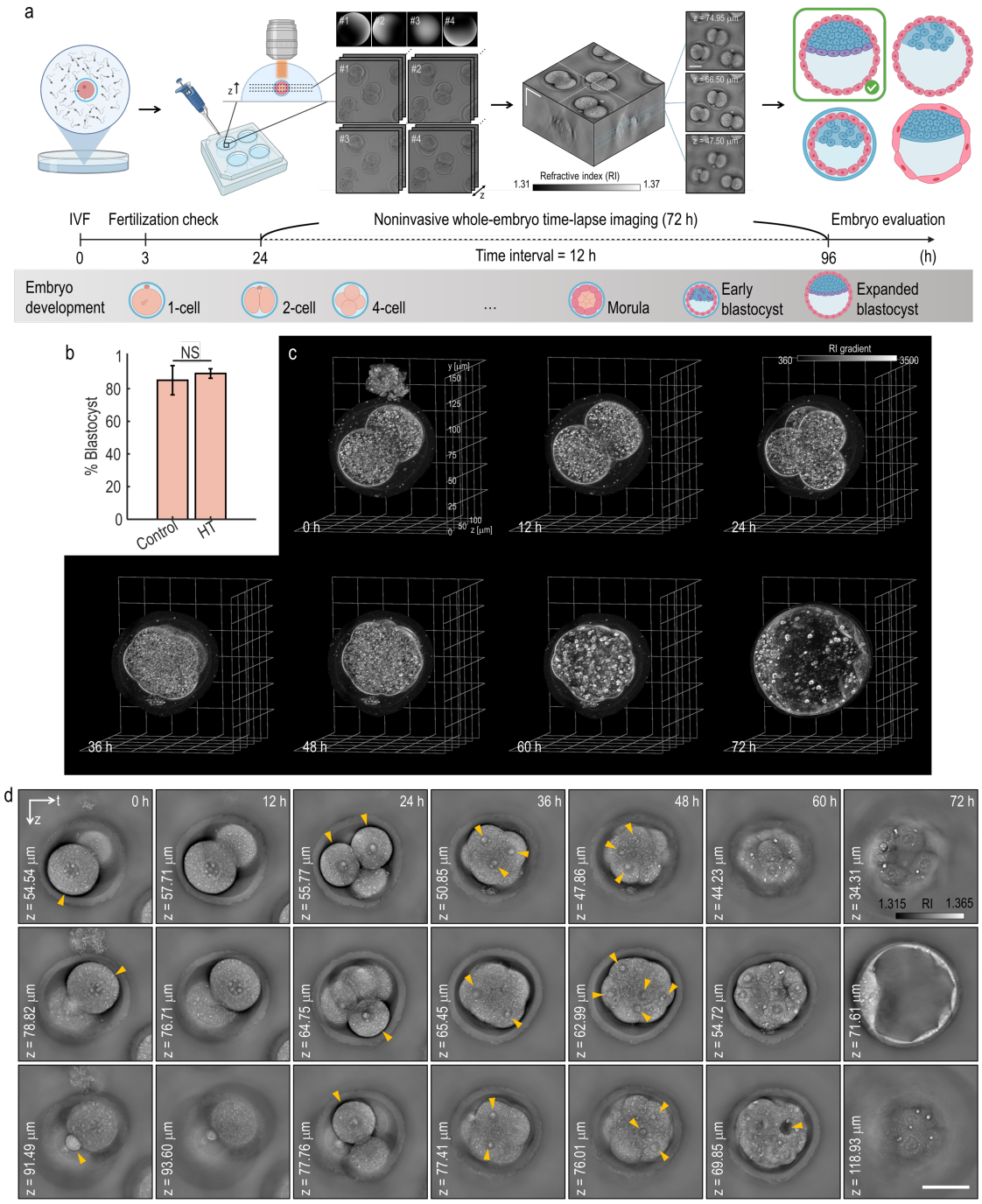


**Fig.1 | Time-lapse low-coherence HT of embryo development in IVF a.** Experimental procedure. The mouse embryos were collected at the 2-cell stage, and were time-lapse monitored for 72 hours from the 2-cell stage to expanded blastocyst using low-coherence HT, followed by 3D morphological assessment of the embryos. In low-coherence HT, multiple intensity images were measured under four optimized illuminations with axial scanning of a sample, after which the measured intensity stack was deconvolved to reconstruct a 3D RI image. **b**. Blastocyst rates were similar between embryos cultured in standard incubator and those time-lapse monitored using low-coherence HT (N = 3 independent experiments; NS,

not significant by unpaired t test). **c**. 3D rendering and **d.** *XY*-sectioned views of representative time-lapse HT images of mouse embryo development. The *XY*-sectioned views show various contents within the embryos in detail, including two blastomeres and polar body at different focal planes ($t = 0$ h, yellow arrow), multiple blastomeres at their focal planes ($t = 24$ h, yellow arrow), multiple nuclei ($t = 36$ h and $t = 48$ h, yellow arrow), cavity formation ($t = 60$ h), and the trophectoderm and inner cell mass of the expanded blastocyst ($t = 72$ h). Scale bar = 50 μm.

**3D visual inspection of subcellular features within embryos of different developmental potential**

We classified the analyzed embryos into two groups based on their developmental outcomes: Grade A embryos, which progressed from the 2-cell stage to expanded blastocysts within 72 hours, and Grade C embryos, which did not reach the blastocyst stage. This categorization revealed distinct subcellular features in the time-lapse HT videos correlating with their developmental trajectories (Fig. 2). Notably, a significant distinction between Grade A and C embryos was the presence of multi-nucleation (Figs. 2a and 2b), previously linked to reduced embryo quality[6].

Leveraging RI for reproducible and quantitative imaging contrast, low-coherence HT significantly surpasses brightfield imaging in contrast and optical sectioning capability. The present method effectively emphasizes abnormalities such as multi-nucleation and elucidates the 3D morphology and spatial distribution of blastomere nuclei and their nucleoli with remarkable clarity (Figs. 2a1 and 2b1). Notably, multi-nucleation was exclusively detected in Grade C embryos, affecting 4.88% of this category. Additionally, low-coherence HT facilitates accurate measurement of blastomere sizes at their focal planes (Figs. 2c and 2d), an essential morphological criterion for clinical evaluation of cleavage-stage embryos. Whereas Grade A embryos generally featured blastomeres of consistent size, a significant size variation among blastomeres was observed in Grade C embryos. It is crucial to acknowledge, however, that blastomeres with both uniform and varied sizes were present in both Grade A and Grade C embryos.

We noted significant differences in 3D cytoplasmic distribution between the two groups (Figs. 2e and 2f). According to the Istanbul Consensus on embryo assessment, the biological implications of cytoplasmic granularity on implantation potential, observable in Day 2 and Day 3 embryos, warrant further study[3]. In our observations, the majority of Grade A embryos displayed a homogeneous cytoplasm (Fig. 2e1), contrasting with Grade C embryos where cytoplasmic granules frequently aggregated into larger clusters (Fig. 2d) or centralized (Fig. 2f1). HT also enabled the visualization of diverse subcellular features across various developmental stages, including nuclei in the morula stage (Fig. 2g), fragmentation in the 2-cell stage embryos (Figs. 2h and 2h1), and the blastocoel cavity, inner cell mass, and trophectoderm in the expanded blastocyst (Fig. 2i). Notably, in Grade C embryos, we identified small pockets with low RI values within the blastomere cytoplasm, though these occurrences were infrequent (Figs. 2j and 2j1, yellow arrows).

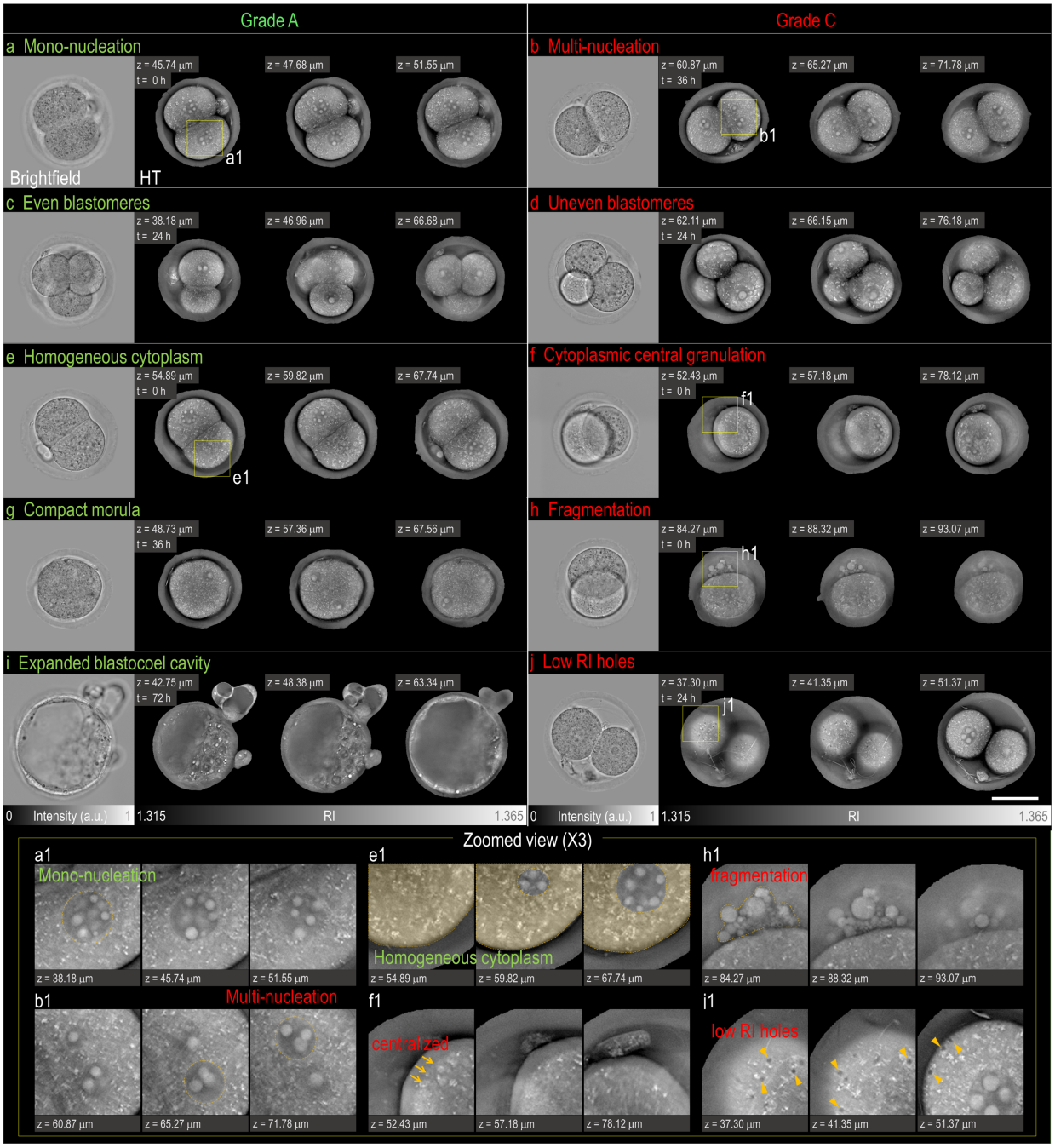


**Fig. 2 | 3D visual inspection of subcellular features within embryos of different developmental potential.** Brightfield (left) and HT images (three *XY*-slices on the right) show **a, b.** mono-nucleation (a) and multi-nucleation (b) in 2-cell embryos; **c, d.** even (c) and uneven (d) blastomeres in 4-cell embryos; **e, f.** homogeneous cytoplasm (e) and centralized cytoplasmic granularity (f) in 2-cell embryos; **g.** compact cell mass in morula; **h.** fragmentation in the 2-cell embryo; **i**. expanded blastocoel cavity, inner cell mass, and trophectoderm in the expanded blastocyst, and **j** cytoplasmic dark holes with low RI values in 2-cell embryos. **a1**–**j1** Zoomed views of the yellow boxes in **a**–**j**. Overall, the images in the left column were of the Grade A embryos, which developed from the 2-cell stage to expanded blastocysts within 72 hours, while

the images in the right column were of the Grade C embryos, which failed to develop into blastocysts. Compared to their brightfield counterparts, HT visualizes the 3D morphology and spatial distribution of subcellular features within embryos at various developmental stages. Scale bars = 50 μm.

**Noninvasive 3D subcellular assessment of embryo quality at *t* = 24 h.**

The developmental paths of embryos categorized by grades became increasingly distinct, particularly 24 hours post-2-cell stage. This observation led us to conduct a deeper analysis at this specific time point (t = 24 h) to pinpoint physiologically significant 3D morpho-kinetic parameters, with a particular focus on the blastomeres and their cytoplasm. Notably, the number and size of blastomeres are key factors in the morphological evaluation of cleavage-stage embryos. To assess blastomeres noninvasively in 3D, we first segmented each blastomere at its focal plane within the 3D images, subsequently isolating the cytoplasm by excluding the nucleus (Fig. 3a) (see the Methods). Figure 3b presents HT images of Grade A and Grade C embryos at t = 24 h, showcasing the segmented blastomeres and their cytoplasm.

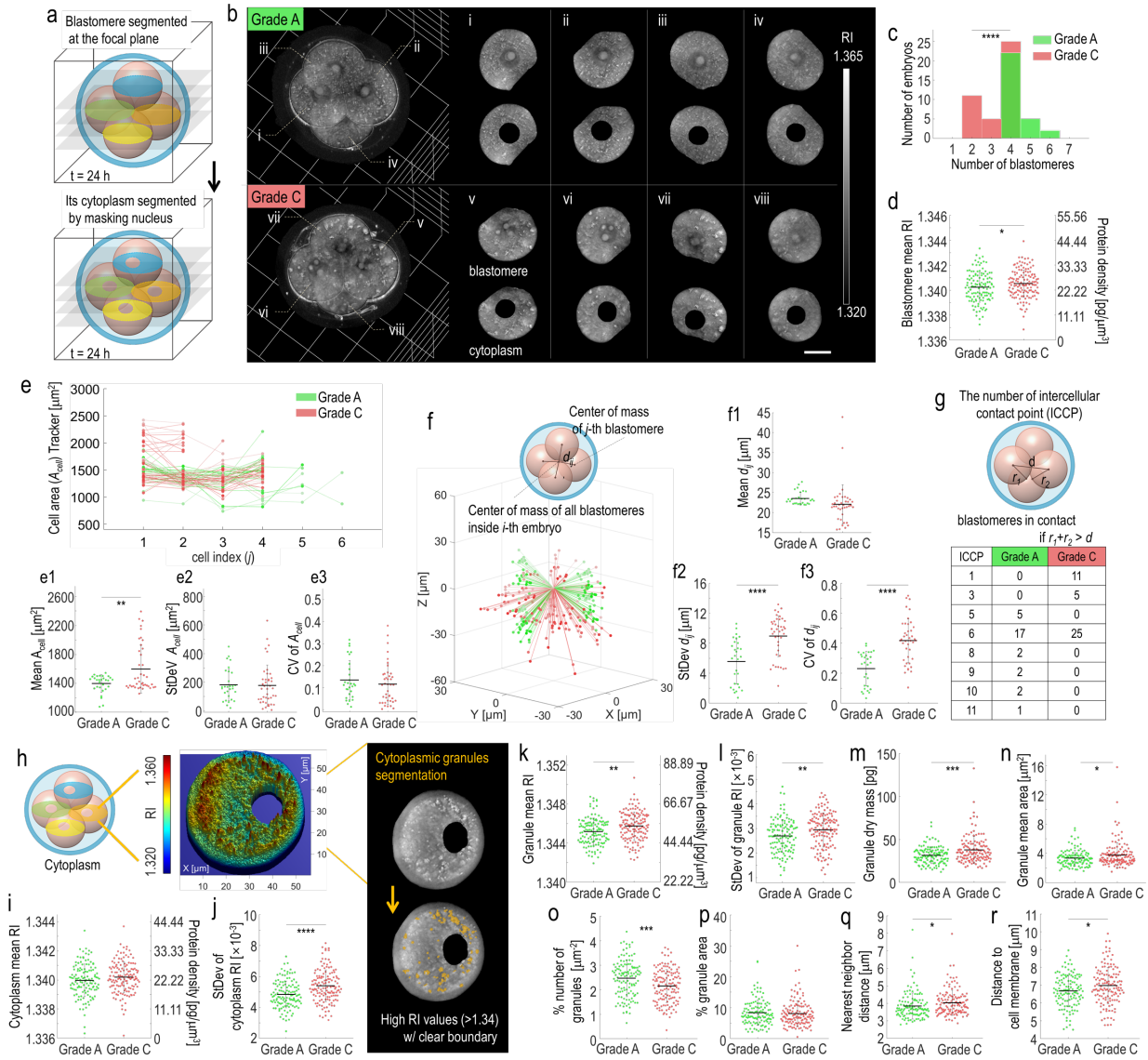


| ICCP | Grade A | Grade C |
|---|---|---|
| 1 | 0 | 11 |
| 3 | 0 | 5 |
| 5 | 5 | 0 |
| 6 | 17 | 25 |
| 8 | 2 | 0 |
| 9 | 2 | 0 |
| 10 | 2 | 0 |
| 11 | 1 | 0 |

**Fig. 3 | Noninvasive 3D subcellular assessment of embryo quality at *t* = 24 h. for embryos at 24 h statistical a.** Schematic representing the segmentation of blastomeres and their cytoplasm at their focal planes in embryos at *t* = 24 h. **b**. Representative HT images of Grade A and Grade C embryos at *t* = 24 h, including the segmented blastomeres (i–iv) and their cytoplasm (v–viii). **c, d.** Comparison of the number (c) and mean RI values (d) of blastomeres between Grade A (green) and Grade C (red) embryos. The mean RI values were presented with the corresponding protein density values. **e–g.** Comparison of the size (e) and 3D spatial arrangement (f, g) of blastomeres between the groups. The size of each blastomere was determined at its focal plane, and its mean (e1), standard deviation (e2) and coefficient of variation (CV) (e3) were compared between the groups. To quantitatively investigate the 3D spatial arrangement of blastomeres, the center of mass of each blastomere was identified, followed by the calculation of displacement between the center of mass of the blastomere of interest and the center of mass of all blastomeres (f). The mean (f1), standard deviation (f2), and CV (f3) of the displacements were then compared between the groups. The number of intercellular contact points (ICCP) within embryos was also estimated and compared between the groups (g). **h–r.** Comparison of cytoplasmic distribution between the groups. The cytoplasmic inner components of high RI values (RI > 1.34) with clear boundaries were determined as cytoplasmic granules (h). The cytoplasmic distributions of the Grade A and Grade C embryos were compared in various features, including the RI mean and standard deviation of the cytoplasm (i, j) and its granules (k, l), dry mass (m), mean area (n), percent number (o) and area (p) of the cytoplasmic granules, nearest neighbor distance between the granules (q), and the distance between the granules and their nearest cell membranes (r). Data were presented from 3 independent experiments, N = 29 Grade A embryos and N = 41 Grade C embryos, n = 125 blastomeres (Grade A) and n = 137 blastomeres (Grade C); **** $p < 0.0001$, *** $p < 0.001$, ** $p < 0.01$, * $p < 0.05$ by unpaired *t*-test. Scale bar = 20 μm.

Utilizing the segmented blastomeres, we initially quantified the number of blastomeres and analyzed their internal contents (Figs. 3c and 3d). Notably, the count of blastomeres varied significantly between the two groups (Fig. 3c), with a distinct disparity in developmental stages at t = 24 h—typically, this stage is expected to be the 4-cell stage in the mouse models under study. Embryos presenting with fewer than four blastomeres demonstrated a generally lower developmental potential. Furthermore, an intriguing discovery was the significantly elevated mean RI values of blastomeres in Grade C embryos (Fig. 3d). Considering RI's direct correlation with protein concentration[40], this finding implies that blastomeres in embryos of lower developmental potential are characterized by higher protein density.

We further examined the size of blastomeres in cleavage-stage embryos (Fig. 3e), a parameter commonly analyzed with standard 2D label-free microscopy in clinical settings[3]. Due to our method's optical sectioning ability, we could accurately measure the size of each blastomere at its specific focal plane. Notably, the average area ($A_{cell}$) of blastomeres was significantly larger in Grade C embryos (Fig. 3e1), reflecting that embryos with lower developmental potential tend to have fewer blastomeres, each taking up more space within the embryo (Fig. 3c). This observation suggests the number of blastomeres may play a more critical role than their individual sizes in assessing embryo quality. To gauge size variability, we computed the standard deviation and coefficient of variation (CV) for blastomere sizes across the groups (Figs. 3e2 and 3e3). Although uneven blastomere size in the 2-, 4-, and 8-cell stages is typically linked to poorer embryo quality, our data showed no significant difference in these size variability metrics between the groups. This finding indicates the need for further research into additional morphological characteristics to more effectively identify embryos with a high developmental potential.

Additionally, we conducted a quantitative analysis of the 3D spatial arrangement of blastomeres (Fig. 3f). We pinpointed the center of mass for each blastomere and computed the displacement between this point and the collective center of mass of all blastomeres within the embryo. Remarkably, while the average displacement did not differ between the groups, the standard deviation and CV of these displacements were markedly higher in Grade C embryos (Figs. 3f1–3f3). These findings indicate that the metrics quantitatively describing the 3D spatial organization could act as novel, noninvasive biomarkers for assessing embryo quality. Typically, embryos poised for successful development tend to exhibit symmetrically arranged blastomeres in terms of both spatial distribution and size. Further exploring the influence of spatial arrangement on embryo quality, we calculated the number of intercellular contact points (ICCPs) within the embryos (Fig. 3g). A criterion was established where two distinct blastomeres were considered in contact if their displacement was less than the combined sum of their radii ($r$), derived from $A_{cell} = \pi r^2$. Consequently, Grade C embryos more commonly exhibited fewer than six ICCPs, reinforcing the notion that diminished cell-cell contact in early-stage embryos might adversely affect subsequent development stages[41].

Subsequently, we carried out a quantitative assessment of the granular structures within the cytoplasm (Figs. 3h–r) to contribute to the evolving field of cytoplasmic scoring in IVF[3]. We identified cytoplasmic granules as entities with RI values greater than 1.34 and distinct boundaries, utilizing a threshold based on the RI value and its gradient, derived from both the original and Sobel-filtered RI images (Fig. 3h). Notably, while the average RI values of the cytoplasm did not vary significantly between groups (Fig. 3i), the average RI values and dry mass of the cytoplasmic granules were markedly higher in Grade C embryos (Figs. 3k and 3m; see the Methods). Furthermore, the variation in RI, for both the cytoplasm and its granules, was significantly greater in Grade C embryos (Figs. 3j and 3i). Additionally, the average size of the granules within the cytoplasm was larger in Grade A embryos (Fig. 3n).

Taken together, our findings suggest that early cleavage-stage embryos with lower developmental potential tend to display a non-homogeneous cytoplasmic distribution, primarily due to the aggregation of cytoplasmic granules. In particular, Grade C embryos exhibited a significantly lower density of cytoplasmic granules per unit area of cytoplasm (Fig. 3o), although the total area occupied by these granules within the cytoplasm showed no significant difference between groups (Fig. 3p). Further scrutiny of their spatial arrangements reinforced this observation, revealing that the average distance between adjacent cytoplasmic granules was notably larger in Grade C embryos (Fig. 3q). Additionally, the separation between cytoplasmic granules and the closest cell membrane was significantly increased in the Grade C embryos (Fig. 3r). This suggests that centralization of cytoplasmic granules might play a role in the observed non-homogeneous distribution of cytoplasm in embryos demonstrating lower developmental potential.

**Noninvasive 3D subcellular assessment of embryo quality at *t* = 36 h.**

We expanded the application of low-coherence HT optical sectioning to explore the morula stage, a phase often overlooked in IVF clinics due to traditionally unclear imaging. Through this approach, we successfully identified individual nuclei in embryos transitioning to the morula stage 36 hours post the 2-cell stage (Fig. 4). To accurately segment the nuclei in three dimensions, we initially acquired multiple 2D masks spanning 3–7 axial planes, ensuring comprehensive coverage of all nucleoli within each nucleus (Figs. 4a and 4b). These masks were then seamlessly integrated along the axial direction to form a cohesive 3D mask (see the Methods section). Figure 4b presents representative 3D HT images of Grade A and Grade C embryos at t = 36 h, with the segmented nuclei highlighted in yellow for enhanced visibility in the 3D

renderings. Additionally, the XY-sectioned views elucidate the intricate 3D spatial arrangement of the nucleoli within the nuclei.

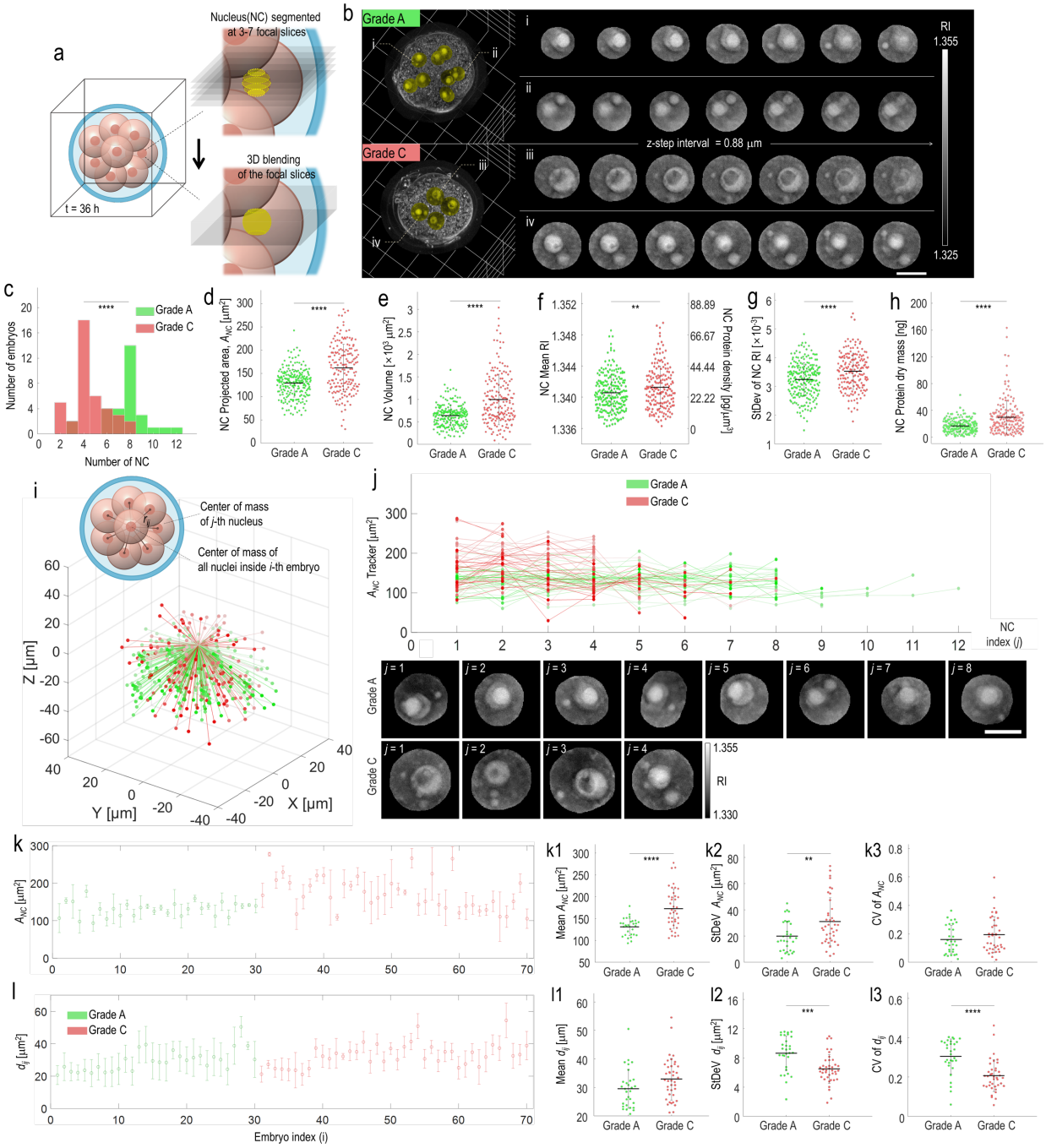


**Fig. 4 | Noninvasive 3D subcellular assessment of embryo quality at *t* = 36 h.** Schematic representing the volumetric segmentation of nuclei in embryos at *t* = 36 h. **b**. Representative HT images of Grade A and Grade C embryos at *t* = 36 h. The segmented nuclei were pseudo-colored in yellow in the 3D rendered views and presented at multiple focal planes for Grade A (i, ii) and Grace C (iii, iv) embryos, respectively. **c–h.** Comparison of the number (c), projected area (d), volume (e), RI mean (f) and standard deviation (g),

and dry mass (g) of nucleus (NC) between Grade A (green) and Grade C (red) embryos. The mean RI values were presented with the corresponding protein density values. **i–l.** Comparison of the size (i, l) and 3D spatial arrangement (j, k) of nuclei between the groups. The maximum intensity projection images of all nuclei within two representative embryos were visualized for each group, respectively (j). The mean (k1), standard deviation (k2) and CV (k3) of the projected areas of nuclei were compared between the groups (k). To quantitatively investigate the 3D spatial arrangement of nuclei, the center of mass of each nucleus was identified, followed by the calculation of displacement between the center of mass of the nucleus of interest and the center of mass of all nuclei (i). The mean (l1), standard deviation (l2), and CV (l3) of the displacements were then compared between the groups (l). Data were presented from 3 independent experiments, N = 30 Grade A embryos and N = 40 Grade C embryos, n= 230 nuclei (Grade A) and n = 179 nuclei (Grade C); ****$p < 0.0001$, ***$p < 0.001$, **$p < 0.01$, *$p < 0.05$ by unpaired *t*-test. Scale bars = 10 μm.

Utilizing the segmented nuclei, we embarked on a comparative analysis of their number, size, and internal composition between the groups (Figs. 4c–h). The quantity of nuclei was notably higher in Grade A embryos (Fig. 4c), while the volume and projected area ($A_{NC}$) of nuclei were significantly larger in Grade C embryos (Figs. 4d and 4e). This pattern indicates that embryos with higher developmental potential experienced more cellular differentiation events in the given timeframe. Furthermore, since the number of nuclei roughly corresponds to the number of blastomeres, it could serve as a novel, noninvasive marker for evaluating the morula stage, a phase characterized by the merging of blastomere boundaries, which complicates blastomere counting. Additionally, both the average and variability in RI values, alongside the dry mass of the nuclei, were substantially elevated in Grade C embryos (Figs. 4f–h). These findings suggest that metrics related to RI might be instrumental for the quantitative evaluation of morula-stage embryos, though additional studies are required to fully understand the implications of these metrics on embryo development.

To elucidate physiologically meaningful 3D morpho-kinetic parameters, we evaluated the size and spatial organization of nuclei within embryos (Figs. 4i–l). Figure 4j displays the projected areas of 3D segmented nuclear volumes, with maximum intensity projection images of nuclei from two representative embryos for each group. The analysis revealed that both the average and variability of the nuclear area ($A_{NC}$) were significantly elevated in Grade C embryos (Figs. 4k1 and 4k2), though no notable difference was found in the CV of nuclear areas between groups (Fig. 4k3). This finding contrasts with the association between uneven cell size and reduced embryo quality[3], suggesting that nuclear size variability at the morula stage may not directly correlate with embryo quality. We also delved into the 3D spatial positioning of nuclei (Figs. 4i and 4l), identifying the center of mass for each nucleus to calculate the displacement relative to the collective center of mass of all nuclei within an embryo (Fig. 4i). Interestingly, while the average displacement did not differ significantly between groups (Fig. 4l1), the standard deviation and CV of these displacements were markedly higher in Grade A embryos (Figs. 4l2 and 4l3). These findings imply that the variability in nuclear displacement could serve as an insightful parameter for morphologically assessing morula-stage embryos.

**Prediction of embryos with high developmental potential using 3D morpho-kinetic parameters**

We further set out to develop a predictive model for blastocyst formation utilizing the identified 3D morpho-kinetic parameters (Fig. 5). The use of artificial intelligence (AI) to standardize the embryo selection process in clinical IVF has seen various approaches[4,42-47], aiming to predict blastocyst quality, implantation,

and pregnancy outcomes based on diverse data inputs. These include morpho-kinetic annotations[5,44], manual morphological assessment of day 5 embryos[45,46], known implantation data (KID)[42,43] or clinical pregnancy outcomes[46], and raw time-lapse videos[47]. Particularly, models leveraging morpho-kinetic annotations have primarily focused on kinetic parameters, such as the timing of cell divisions and the duration of cell cycles, for the hierarchical classification of embryos. Concurrently, assessments of 2D morphology, such as uneven blastomeres and multinucleation, have been integral for the preliminary screening of nonviable embryos[5,44].

To demonstrate the effectiveness of HT in creating a predictive model for blastocyst formation, we constructed a decision tree ensemble model. This model, which predicts blastocyst formation, utilizes 3D morphological parameters identified at t = 24 h and t = 36 h (Fig. 5a). The decision tree ensemble method was selected to reduce the risk of overfitting the training data[48]. We incorporated a diverse array of 33 morpho-kinetic parameters from 69 embryos to build an ensemble composed of 100 individual decision trees, effectively categorizing the embryos into Grade A and Grade C. During the K-fold cross-validation (K = 10), the model demonstrated impressive performance metrics, achieving a prediction accuracy of 0.9143, precision of 0.9500, recall of 0.8667, and an F1 score of 0.8814.

To provide a deeper understanding of the classification process at a subcellular level, Fig. 5a outlines three exemplary trees from the ensemble model. These trees incorporate comprehensive analyses, including the 3D spatial organization of cells and nuclei (e.g., the average cell displacement at t = 24 h and the CV of nuclear displacement at t = 36 h), as well as the internal makeup of subcellular structures (e.g., the variability in cytoplasm RI at t = 24 h and the dry mass of nucleus at t = 36 h). Interestingly, despite the absence of significant differences in the univariate analysis (Fig. 3), the variability in blastomere sizes (i.e., CV of cell area), a critical factor in conventional embryo assessments, played a role in the classification. This suggests that further exploration into the nonlinear and interactive influences of these morpho-kinetic parameters could significantly enhance our comprehension of embryo development.

| Random forest generated from | All features | 5 selected features | Conventional |
|---|---|---|---|
| Prediction accuracy | 0.9143 | 0.9571 | 0.8857 |
| Precision | 0.9500 | 0.9500 | 0.8833 |
| Recall | 0.8667 | 0.9667 | 0.8667 |
| F1 Score | 0.8814 | 0.9514 | 0.8648 |

**Fig. 5 | Prediction of embryos with high developmental potential using 3D morpho-kinetic parameters.** **a.** Schematic of a proposed decision tree ensemble model as a predictive model for blastocyst formation. The three exemplar trees within the ensemble model are described in detail, where the 3D morpho-kinetic parameters identified at $t = 24$ h and $t = 36$ h are used for the hierarchical classification of embryos into two groups of Grade A and Grade C. **b.** The overall distribution of the embryos visualized in a 2D feature space using t-SNE. **c.** Histogram plot of the linear projection of embryos for effective classification using LDA. **d.** The evaluation of feature importance for a total of 33 morpho-kinetic parameters used in the proposed ensemble model. **e.** Schematic of an approximated single decision tree generated using 5 selected features in (d). To emphasize the predictive power of 3D morpho-kinetic parameters, the K-fold cross-validation was performed for three independent ensemble models generated using all features, 5 selected features, and features that can be extracted using conventional 2D label-free microscopy image. Data were presented from 3 independent experiments, N = 29 Grade A embryos and N = 40 Grade C embryos.

To visualize the distribution of embryos classified as Grade A and C effectively, we utilized the t-stochastic neighbor embedding (t-SNE) algorithm and linear discriminant analysis (LDA) (Figs. 5b and 5c). The t-

SNE method facilitated the transformation of high-dimensional data into a more comprehensible lower-dimensional space while maintaining the integrity of the data's local structure. This approach yielded a clear distinction between the two groups (Fig. 5b). Subsequently, LDA was employed to enhance our understanding of the classification efficacy of the identified 3D morpho-kinetic parameters. In contrast to t-SNE, LDA seeks to identify the optimal linear projection that maximizes the separation between high-dimensional datasets. As anticipated, LDA provided a more pronounced demarcation between the embryo groups than the separation achieved with t-SNE (Fig. 5c).

We further evaluated the predictive capability of the 3D morpho-kinetic parameters by analyzing feature importance within the ensemble model (Fig. 5d). Feature importance was determined using MATLAB's 'predictorImportance' function, which essentially measures the impact of each split on enhancing the model's classification accuracy. Within the ensemble framework, the significance of each feature is cumulatively assessed across all decision trees to gauge its overall contribution to the model. Notably, the parameters associated with the 3D spatial organization of cells at t = 24 are highly influential in the classification, ranking the first, third, and fourth in importance for the mean, standard deviation, and CV of cell 3D displacement, respectively. It was also found that the number and size of nuclei at t = 36 h were also included in the five most influential features, indicating that 3D subcellular features could significantly contribute to the classification.

To highlight the predictive capabilities of 3D morpho-kinetic parameters in embryo selection, we further identified the five features that maximize the prediction accuracy: (1) the CV of cell 3D displacement, (2) the average cell 3D displacement at t = 24 h, (3) the standard deviation of nuclear 3D displacement, (4) the standard deviation of nuclear area at t = 36 h, and (5) the number of ICCPs at t = 24 h. Leveraging these features, we devised an approximate single decision tree to elucidate the hierarchical classification of embryos, offering a detailed 3D subcellular perspective (Fig. 5e). In our study involving mouse embryos, those characterized by (i) displaying evenly distributed blastomeres at t = 24 h, (ii) having at least 4 ICCPs, and (iii) having nuclei of similar size at t = 36 h were classified as Grade A. We conducted K-fold cross-validation (K = 10) on three distinct ensemble models: one using all identified features, another using the 5 selected features, and a third employing features obtainable from traditional 2D label-free microscopy. For the model based on conventional microscopy, we selected features such as cell number, average cell size, standard deviation, CV of cell size, and the count of ICCPs at t = 24 h. The models achieved prediction accuracies of 0.9143, 0.9571, and 0.8857 for the all-features, 5-selected-features, and conventional-features models, respectively.

These findings indicate that the identified 3D morpho-kinetic parameters significantly enhance the accuracy of selecting viable embryos, providing a valuable supplement to existing 2D morpho-kinetic assessments. Notably, the model utilizing the 5 selected features outperformed the one considering all features, suggesting a more targeted feature set might yield superior predictive outcomes. Further exploration into optimizing feature selection could refine the relationship between these 3D morpho-kinetic parameters and embryo development, thereby facilitating the advancement of embryo selection methodologies.

## Discussion

Here, we introduce the use of low-coherence HT for conducting high-resolution, time-lapse 3D evaluations of unlabeled mouse embryos during the critical phases of embryogenesis *in vitro*. This study underscores the utility of 3D spatiotemporal profiling in facilitating an accurate, noninvasive assessment of embryo quality. We uncover distinct 3D cellular and subcellular features that markedly differ between embryos of

high and low developmental potential. Typically, by t = 24 h, embryos are expected to possess four blastomeres of uniform size and distribution within a 3D space, coupled with a homogeneous cytoplasm. At t = 36 h, embryos are anticipated to progress to the morula stage, characterized by the blurring of blastomere boundaries, containing an average of ~~at least~~ eight nuclei, and displaying high variability in the 3D nuclear distribution in comparison to embryos of lesser developmental potential. Leveraging the exceptional optical sectioning capabilities of low-coherence HT, our analysis is poised to expand to additional intra-embryonic structures, including the polar body, blastomeres at the 2-cell stage, and the trophectoderm and inner cell mass of expanded blastocysts.

Our research utilizing mouse models establishes a foundational approach for the high-resolution, 3D examination of human embryo development, offering nuanced subcellular insights into the early stages of embryogenesis. We introduce a structured analysis framework for the quantitative evaluation of the cytoplasm in cleavage-stage embryos, with a special emphasis on identifying cytoplasmic granules characterized by high RI values indicative of elevated protein density. Anticipating further research on human embryos, we aim to enhance our comprehension of the impact of cytoplasmic heterogeneity on the initial phases of embryo development, which could pave the way for the widespread implementation of cytoplasmic scoring during the cleavage stage[3]. Additionally, our techniques allow for the quantitative analysis of 3D nuclear morphology and spatial arrangements during the morula stage, a period traditionally overlooked in embryo assessments due to imaging challenges, thereby restricting morphological evaluations to compaction status based on embryo volume[3]. We believe that our proposed framework for nuclear assessment in morula-stage embryos could be tailored for application in day 4 embryo evaluations, thereby enabling detailed subcellular level analysis.

We highlight the crucial role of multivariate analysis in evaluating the proposed 3D morpho-kinetic parameters for their impact on embryo quality assessment. By analyzing 33 morphological parameters identified at t = 24 h and t = 36 h, we developed a decision tree ensemble model to forecast developmental outcomes, such as blastocyst formation. This approach allowed us to assess the influence of each parameter on prediction outcomes, revealing that some parameters, which did not show significant differences in univariate analysis (like the size variability of blastomeres at t = 24 h), were nonetheless influential in the hierarchical classification of embryos on a 3D subcellular level. Furthermore, we observed an enhancement in prediction accuracy of the ensemble model: utilizing all features yielded an accuracy of 0.9143, an improvement over the 0.8857 accuracy achieved with features identifiable through conventional 2D label-free microscopy. This accuracy further increased to 0.9571 when employing five selected features, mostly associated with the 3D spatial arrangement of cells and nuclei. Moving forward, a thorough examination of the nonlinear and interactive dynamics among these 3D morpho-kinetic parameters could refine our feature selection process, thereby enhancing the model's predictive precision. For example, we found that embryos with high developmental potential exhibited high variability in the nuclear 3D distribution at t = 36 h, despite the uniform distribution of cells at t = 24 h. To address these seemingly contradictory results, further research could investigate the interactive effects of parameters that may influence the spatial organization within the limited space of embryos, such as the number and size of cells and nuclei.

Incorporating the dynamic aspects of live embryos will enrich the set of developmental indicators available, such as the timing of cleavage, the duration of the cell cycle, and the synchrony of cell divisions[5]. Currently, in our system, to minimize the total light energy dose exposed to embryos, the imaging interval for time-lapse recordings is set at 12 hours. This is despite the high temporal resolution of low-coherence HT, which can capture images every 7 seconds, allowing for continuous monitoring of embryo development. Further reductions in light exposure could be achieved in two ways: by lowering the light intensity for each

XY-slice or by reducing the number of XY-slices needed to compile a complete 3D RI image. The former can be implemented by using a camera with high enough signal-to-noise ratio to detect lower light levels effectively. More complex modifications could address the latter, such as altering the illumination schemes[49] or applying spectral-multiplexing to optimize illuminations[50]. These adjustments aim to refine the balance between image quality and embryo safety, enhancing the practicality of using HT in sensitive developmental studies.

We foresee our methodology serving as a cornerstone for the development of fully automated, unmanned systems for handling, culturing, and selecting optimal embryos for IVF. To enhance the efficiency and scalability of our demonstration, it is feasible to automate several currently manual processes. For instance, the manual segmentation of subcellular organelles from 3D RI tomograms could be replaced by AI-driven automation, ensuring objective and consistent analysis across a wider array of subcellular features, independent of the operator's expertise with holotomography[51-53]. Additionally, integrating virtual staining techniques with our approach could provide detailed, molecule-specific insights into unlabeled embryos throughout their development[54]. With the swift progression of AI-enhanced HT technologies[55], we anticipate the practical application of this advanced 3D subcellular analysis in clinical settings, facilitated by AI's capability to accurately track blastomeres, cytoplasm, and nuclei during the embryonic development process.

## Methods

### Embryo culture

For conventional IVF, 4-week-old F1 (C57BL/6 X DBA/2) females and 10-week-old F1 (C57BL/6 X C3H) males, as well as 10-week-old BALB/c females and 8-week-old BALB/c males were obtained from Orient Bio Inc. (Sungnam, South Korea). While the hybrid mice were used to conduct mouse embryo assay of low-coherence HT, the inbred mice were used for the proposed noninvasive analysis. The animals were provided with rodent chow and reverse osmosis water. All experiments were conducted at the Korea Advanced Institute of Science and Technology, in accordance with the procedures approved by the Institutional Animal Care and Usage Committee (IACUC) (KA2023-005-v4). Female mice received an intraperitoneal (I.P.) injection of 0.1 ml ultra-superovulation reagent (CARD Hyperova; Cosmo Bio, Japan), followed by 20 IU of human chorionic gonadotrophin I.P. (hCG; Sigma-Aldrich, USA) 48 h later. At 15-18 h post-hCG, female mice were culled via cervical dislocation and oviducts were dissected, while male mice were also culled via cervical dislocation and epididymal caudal tubes were dissected. From the dissected oviducts, cumulus mass and oocytes were collected and cultured within an 100 μl drop of human tubal fluid (HTF; Cosmo Bio, Japan) overlaid with 10 ml of mineral oil (GeorgiaChem, Korea) in a fertilization dish. Collected sperms were cultured within a 100 μl drop of preincubation medium (PM; Cosmo Bio, Japan) overlaid with 10 ml of mineral oil (GeorgiaChem, South Korea) in a sperm culture dish for 30 min. Fertilization was then conducted by dispensing 3 μl of sperm-containing PM medium into the HTF medium with the oocytes in the fertilization dish. At 3 h post-fertilization, zygotes were collected and washed three times in a washing dish containing four drops of 80 μl HTF overlaid with 10 ml of mineral oil. The zygotes were then cultured in a standard incubator for 21 h. After incubation, 2-cell embryos were collected and transferred into two independent Oosafe 4-well dishes (SparMed, Denmark) for imaging and control group, respectively. In each well, 20-30 embryos were cultured within 20 μl of KSOM medium (Cosmo Bio, Japan) overlaid with 0.8 ml of mineral oil. The dishes were stored into an incubation chamber

(Tokai Hit, Japan) within the low-coherence HT or standard incubator, which was maintained at 37°C with 5% $CO_2$ in a humidified environment.

**Low-coherence HT of mouse preimplantation embryo development**

To monitor the development of mouse preimplantation embryos, we utilized a specialized low-coherence HT system (HT-X1, Tomocube), specifically tailored for embryo imaging (see Supplementary Fig. 1 and Note 1). This system captures transmitted light through the sample using four optimized illumination patterns, enabling the reconstruction of 3D RI images through the process of 3D deconvolution of the captured intensity data. The optical setup incorporates a light-emitting diode (LED; LE A Q8WP, OSRAM) emitting at a peak wavelength of 624 nm, serving as the low-coherence light source. The collimated LED light is modulated in the Fourier plane by a digital micro-mirror device (DMD; DLP4500, Texas Instrument), and then directed through a relay lens (CPL150, Tomocube), which projects the patterned illumination onto the back focal plane of a condenser lens with a numerical aperture (NA) of 0.72 (CWD30, Tomocube).

The illuminations were then projected onto the sample plane using the condenser lens. The illumination intensity was measured to be 13.36 $W/m^2$ at the sample plane using an optical power meter (PM100D, Thorlabs). The total light energy dose exposed to the embryos during time-lapse imaging was 1.8 $kJ/m^2$, which is sufficiently small compared to previously reported values for safe measurement using red illumination. The transmitted light through the sample was imaged on a CMOS camera (FS-U3-28S5, FLIR) using an objective lens with an NA of 0.7 (UCPLFLN20X, Olympus) and a tube lens (AC508-180-A). A total of 480 intensity images were captured under four optimized illuminations with axial scanning to obtain a single 3D RI image of $238 \times 238 \times 125$ $\mu m^3$ volume. The RI images offer a lateral and axial resolution of 176 nm and 1.09 μm, respectively. To cover the entire region occupied by the group-cultured embryos, wide-field RI images ($1.5 \times 1.5$ $mm^2$ field of view) were obtained by stitching $7 \times 7$ tiles. Using the present method, time-lapse imaging of mouse preimplantation embryo development was conducted for 72 hours, from the 2-cell stage to expanded blastocyst, at 12-hour intervals in both brightfield and HT mode. A total of 71 time-lapse HT videos were obtained from 3 independent experiments, including 30 embryos in the Grade A group and 41 embryos in the Grade C group, respectively. 1–2 HT images acquired incorrectly—for example, those acquired when embryos were severely moving during tile imaging, were further excluded from the analysis.

**3D segmentation method in HT images**

For the 3D segmentation of blastomeres and their subcellular structures, we applied Segment Anything (SAM; https://segment-anything.com/), an open-source image segmentation model developed by Meta AI. To remain a single embryo within the field of view, we first segmented each embryo from the wide-field RI images of the group-culture embryos. For each embryo, we obtained multiple 2D masks of the embryo at 15–20 axial planes using SAM and manual segmentation. While SAM enabled accurate segmentation of the embryo at in-focus planes, manual segmentation was necessary at out-of-focus planes where the embryo boundaries became obscured. We then smoothly blended the segmented *XY*-slices along the axial direction using the blendedPolymask function written in Matlab[56], creating a 3D mask. The segmentation of blastomeres was sequentially conducted at their focal planes using SAM. Nuclei segmentation was conducted in the similar manner as in embryos. We segmented each nucleus at 3–7 axial planes manually, followed by smoothing the segmented *XY*-slices along the axial direction to create a 3D mask.

## Dry mass calculation

The dry mass can be calculated from the linear relation between the RI and mass density of dry protein, $n(\mathbf{r}) = n_m + \alpha C(\mathbf{r})$. Here, $n(\mathbf{r})$ represents the mean RI of the sample, $n_m$ is the RI of the KSOM medium (approximated to 1.336), $\alpha$ is the RI increment, and $C(\mathbf{r})$ denotes the protein density. We first determined the protein density of blastomeres and their subcellular structures from their mean RI values with $\alpha$ set at 0.18 ml $g^{-1}$, a typical value for most proteins. The dry mass was then calculated by multiplying the protein density by the volume, which was determined by the segmented mask.


## Acknowledgement

This work was supported by National Research Foundation of Korea (2015R1A3A2066550, 2022M3H4A1A02074314), Basic Science Research Program through the National Research Foundation of Korea (NRF) funded by the Ministry of Education (RS-2023-00241278), a grant of the Korea Health Technology R&D Project through the Korea Health Industry Development Institute (KHIDI) funded by the Ministry of Health & Welfare (HR22C1605), Institute of Information & communications Technology Planning & Evaluation (IITP; 2021-0-00745) grant funded by the Korea government (MSIT), KAIST Institute of Technology Value Creation, Industry Liaison Center (G-CORE Project) grant funded by MSIT (N11230131).


## Competing interests

G.P., J.H.P., J.P.D., and Y.K.P. have financial interests in Tomocube, a company that commercializes HT and QPI products. All other authors declare no competing interests.

## References


1 *2021 National ART Summary*, <https://www.cdc.gov/art/reports/2021/summary.html#table> (2023).

2 Gardner, D. K., Lane, M., Stevens, J., Schlenker, T. & Schoolcraft, W. B. Blastocyst score affects implantation and pregnancy outcome: towards a single blastocyst transfer. *Fertility and Sterility* **73**, 1155-1158, doi:https://doi.org/10.1016/S0015-0282(00)00518-5 (2000).

3 Alpha Scientists in Reproductive, M. & Embryology, E. S. I. G. o. The Istanbul consensus workshop on embryo assessment: proceedings of an expert meeting†. *Human Reproduction* **26**, 1270-1283, doi:10.1093/humrep/der037 (2011).

4 Dolinko, A. V. & Racowsky, C. in *In Vitro Fertilization: A Textbook of Current and Emerging Methods and Devices* (eds Zsolt Peter Nagy, Alex C. Varghese, & Ashok Agarwal) 227-245 (Springer International Publishing, 2019).

5 Meseguer, M. *et al.* The use of morphokinetics as a predictor of embryo implantation†. *Human Reproduction* **26**, 2658-2671, doi:10.1093/humrep/der256 (2011).

6 Gardner, D. K. & Balaban, B. Assessment of human embryo development using morphological criteria in an era of time-lapse, algorithms and 'OMICS': is looking good still important? *Molecular Human Reproduction* **22**, 704-718, doi:10.1093/molehr/gaw057 (2016).

7 Squirrell, J. M., Wokosin, D. L., White, J. G. & Bavister, B. D. Long-term two-photon fluorescence imaging of mammalian embryos without compromising viability. *Nature Biotechnology* **17**, 763-767, doi:10.1038/11698 (1999).

8 McDole, K. *et al.* In Toto Imaging and Reconstruction of Post-Implantation Mouse Development at the Single-Cell Level. *Cell* **175**, 859-876.e833, doi:https://doi.org/10.1016/j.cell.2018.09.031 (2018).

9 Domingo-Muelas, A. *et al.* Human embryo live imaging reveals nuclear DNA shedding during blastocyst expansion and biopsy. *Cell* **186**, 3166-3181.e3118, doi:https://doi.org/10.1016/j.cell.2023.06.003 (2023).
10 Yu, L. *et al.* Blastocyst-like structures generated from human pluripotent stem cells. *Nature* **591**, 620-626, doi:10.1038/s41586-021-03356-y (2021).
11 Yu, L. *et al.* Large-scale production of human blastoids amenable to modeling blastocyst development and maternal-fetal cross talk. *Cell Stem Cell* **30**, 1246-1261.e1249, doi:10.1016/j.stem.2023.08.002 (2023).
12 Park, Y., Depeursinge, C. & Popescu, G. Quantitative phase imaging in biomedicine. *Nature Photonics* **12**, 578-589, doi:10.1038/s41566-018-0253-x (2018).
13 Lee, S.-A. *et al.* OASL phase condensation induces amyloid-like fibrillation of RIPK3 to promote virus-induced necroptosis. *Nature Cell Biology* **25**, 92-107 (2023).
14 Kim, T. *et al.* RNA-mediated demixing transition of low-density condensates. *Nature Communications* **14**, 2425 (2023).
15 Esposito, M. *et al.* TGF-β-induced DACT1 biomolecular condensates repress Wnt signalling to promote bone metastasis. *Nature cell biology* **23**, 257-267 (2021).
16 Kim, G. *et al.* Rapid species identification of pathogenic bacteria from a minute quantity exploiting three-dimensional quantitative phase imaging and artificial neural network. *Light: Science & Applications* **11**, 190 (2022).
17 Choi, S. Y., Oh, J., Jung, J., Park, Y. & Lee, S. Y. Three-dimensional label-free visualization and quantification of polyhydroxyalkanoates in individual bacterial cell in its native state. *Proceedings of the National Academy of Sciences* **118**, e2103956118 (2021).
18 Ahn, J. H. *et al.* Enhanced succinic acid production by Mannheimia employing optimal malate dehydrogenase. *Nature communications* **11**, 1970 (2020).
19 Wang, L., Li, M. & Hwang, T. H. The 3D Revolution in Cancer Discovery. *Cancer Discovery* **14**, 625-629 (2024).
20 Sung, M. *et al.* Three-dimensional label-free morphology of CD8+ T cells as a sepsis biomarker. *Light: Science & Applications* **12**, 265 (2023).
21 Lee, M. *et al.* Deep-learning-based three-dimensional label-free tracking and analysis of immunological synapses of CAR-T cells. *Elife* **9**, e49023 (2020).
22 Bogdanov, G., Chatterjee, A., Makeeva, N., Farrukh, A. & Gorodetsky, A. A. Squid leucophore-inspired engineering of optically dynamic human cells. *Iscience* **26** (2023).
23 Jung, Y., Wen, L., Altman, A. & Ley, K. CD45 pre-exclusion from the tips of T cell microvilli prior to antigen recognition. *Nature communications* **12**, 3872 (2021).
24 Lee, C. *et al.* Label-free three-dimensional observations and quantitative characterisation of on-chip vasculogenesis using optical diffraction tomography. *Lab on a Chip* **21**, 494-501, doi:10.1039/D0LC01061H (2021).
25 Kang, S. H. *et al.* Interactions of Nanoparticles with Macrophages and Feasibility of Drug Delivery for Asthma. *Int J Mol Sci* **23**, doi:10.3390/ijms23031622 (2022).
26 Mahn Jae, L. *et al.* Long-term three-dimensional high-resolution imaging of live unlabeled small intestinal organoids using low-coherence holotomography. *bioRxiv*, 2023.2009.2016.558039, doi:10.1101/2023.09.16.558039 (2023).
27 Herve, H. *et al.* Multiscale label-free volumetric holographic histopathology of thick-tissue slides with subcellular resolution. *Advanced Photonics* **3**, 026004, doi:10.1117/1.AP.3.2.026004 (2021).
28 Abraham, T. M. *et al.* Label- and slide-free tissue histology using 3D epi-mode quantitative phase imaging and virtual hematoxylin and eosin staining. *Optica* **10**, 1605-1618, doi:10.1364/OPTICA.502859 (2023).
29 Lee, A. J. *et al.* Volumetric Refractive Index Measurement and Quantitative Density Analysis of Mouse Brain Tissue with Sub-Micrometer Spatial Resolution. *Advanced Photonics Research* **4**, 2300112, doi:https://doi.org/10.1002/adpr.202300112 (2023).

30 Chen, M., Tian, L. & Waller, L. 3D differential phase contrast microscopy. *Biomed. Opt. Express* **7**, 3940-3950, doi:10.1364/BOE.7.003940 (2016).

31 Nguyen, T. H., Kandel, M. E., Rubessa, M., Wheeler, M. B. & Popescu, G. Gradient light interference microscopy for 3D imaging of unlabeled specimens. *Nature Communications* **8**, 210, doi:10.1038/s41467-017-00190-7 (2017).

32 Karnowski, K. *et al.* Optical coherence microscopy as a novel, non-invasive method for the 4D live imaging of early mammalian embryos. *Scientific Reports* **7**, 4165, doi:10.1038/s41598-017-04220-8 (2017).

33 Chowdhury, S. *et al.* High-resolution 3D refractive index microscopy of multiple-scattering samples from intensity images. *Optica* **6**, 1211-1219, doi:10.1364/OPTICA.6.001211 (2019).

34 Pierré, W. *et al.* 3D time-lapse imaging of a mouse embryo using intensity diffraction tomography embedded inside a deep learning framework. *Appl. Opt.* **61**, 3337-3348, doi:10.1364/AO.453910 (2022).

35 Li, Z. *et al.* Biodynamic digital holographic speckle microscopy for oocyte and embryo metabolic evaluation. *Appl. Opt.* **60**, A222-A233, doi:10.1364/AO.404298 (2021).

36 Dwapanyin, G. O. *et al.* Investigation of refractive index dynamics during in vitro embryo development using off-axis digital holographic microscopy. *Biomed. Opt. Express* **14**, 3327-3342, doi:10.1364/BOE.492292 (2023).

37 Hugonnet, H., Lee, M. & Park, Y. Optimizing illumination in three-dimensional deconvolution microscopy for accurate refractive index tomography. *Opt. Express* **29**, 6293-6301, doi:10.1364/OE.412510 (2021).

38 Li, R. *et al.* Effect of red light on the development and quality of mammalian embryos. *J Assist Reprod Genet* **31**, 795-801, doi:10.1007/s10815-014-0247-7 (2014).

39 *Mouse Embryo Assay for Assisted Reproduction Technology Devices*, <https://www.fda.gov/regulatory-information/search-fda-guidance-documents/mouse-embryo-assay-assisted-reproduction-technology-devices> (2021).

40 Barer, R. Interference Microscopy and Mass Determination. *Nature* **169**, 366-367, doi:10.1038/169366b0 (1952).

41 Liu, Y., Chapple, V., Feenan, K., Roberts, P. & Matson, P. Clinical significance of intercellular contact at the four-cell stage of human embryos, and the use of abnormal cleavage patterns to identify embryos with low implantation potential: a time-lapse study. *Fertility and Sterility* **103**, 1485-1491.e1481, doi:https://doi.org/10.1016/j.fertnstert.2015.03.017 (2015).

42 Petersen, B. M., Boel, M., Montag, M. & Gardner, D. K. Development of a generally applicable morphokinetic algorithm capable of predicting the implantation potential of embryos transferred on Day 3. *Human Reproduction* **31**, 2231-2244, doi:10.1093/humrep/dew188 (2016).

43 Fordham, D. E. *et al.* Embryologist agreement when assessing blastocyst implantation probability: is data-driven prediction the solution to embryo assessment subjectivity? *Hum Reprod* **37**, 2275-2290, doi:10.1093/humrep/deac171 (2022).

44 Basile, N. *et al.* The use of morphokinetics as a predictor of implantation: a multicentric study to define and validate an algorithm for embryo selection. *Human Reproduction* **30**, 276-283, doi:10.1093/humrep/deu331 (2015).

45 Wang, S., Zhou, C., Zhang, D., Chen, L. & Sun, H. A Deep Learning Framework Design for Automatic Blastocyst Evaluation With Multifocal Images. *IEEE Access* **9**, 18927-18934, doi:10.1109/ACCESS.2021.3053098 (2021).

46 VerMilyea, M. *et al.* Development of an artificial intelligence-based assessment model for prediction of embryo viability using static images captured by optical light microscopy during IVF. *Human Reproduction* **35**, 770-784, doi:10.1093/humrep/deaa013 (2020).

47 Tran, D., Cooke, S., Illingworth, P. J. & Gardner, D. K. Deep learning as a predictive tool for fetal heart pregnancy following time-lapse incubation and blastocyst transfer. *Human Reproduction* **34**, 1011-1018, doi:10.1093/humrep/dez064 (2019).

48 Berntsen, J., Rimestad, J., Lassen, J. T., Tran, D. & Kragh, M. F. Robust and generalizable embryo selection based on artificial intelligence and time-lapse image sequences. *PLOS ONE* **17**, e0262661, doi:10.1371/journal.pone.0262661 (2022).

49 Hugonnet, H., Lee, M. J. & Park, Y. K. Quantitative phase and refractive index imaging of 3D objects via optical transfer function reshaping. *Opt. Express* **30**, 13802-13809, doi:10.1364/OE.454533 (2022).

50 Lee, C. *et al.* Single-shot refractive index slice imaging using spectrally multiplexed optical transfer function reshaping. *Opt. Express* **31**, 13806-13816, doi:10.1364/OE.485559 (2023).

51 Jo, Y. *et al.* Label-free multiplexed microtomography of endogenous subcellular dynamics using generalizable deep learning. *Nature Cell Biology* **23**, 1329-1337, doi:10.1038/s41556-021-00802-x (2021).

52 Park, J. *et al.* Artificial intelligence-enabled quantitative phase imaging methods for life sciences. *Nature Methods* **20**, 1645-1660, doi:10.1038/s41592-023-02041-4 (2023).

53 Goswami, N. *et al.* EVATOM: an optical, label-free, machine learning assisted embryo health assessment tool. *Communications Biology* **7**, 268, doi:10.1038/s42003-024-05960-w (2024).

54 Jo, Y. *et al.* Label-free multiplexed microtomography of endogenous subcellular dynamics using generalizable deep learning. *Nat Cell Biol* **23**, 1329-1337, doi:10.1038/s41556-021-00802-x (2021).

55 Park, J. *et al.* Artificial intelligence-enabled quantitative phase imaging methods for life sciences. *Nature Methods* **20**, 1645-1660 (2023).

56 Sven. *Blended 3D poly2mask*, <https://www.mathworks.com/matlabcentral/fileexchange/37863-blended-3d-poly2mask> (2024).